Chapter 3
Numerical Platform

Keita Yoshioka, Mathias Nest, Daniel Pötschke, Amir Shoarian Sattari, Patrick Schmidt, and David Krach

An essential scientific goal of the GeomInt project is the analysis of potentials and limitations of different numerical approaches for the modelling of discontinuities in the rocks under consideration in order to improve the understanding of methods and their synergies with regard to theoretical and numerical fundamentals. As numerical methods, the "Lattice Element Method" (LEM), the non-continuous discontinuum methods "Discrete Element Method" (DEM), the "Smoothed Particle Hydrodynamics" (SPH), the "Forces on Fracture Surfaces" (FFS) as well as the continuum approaches "Phase-Field Method" (PFM), "Lower-Interface-Method" (LIE), "Non-Local Deformation" (NLD) and the "Hybrid-Dimensional Finite-Element-Method" (HDF) will be systematically investigated and appropriately extended based on experimental results (Fig. 3.1).

The numerical methods in Fig. 3.1 are displayed in accordance to the scale-ability, i.e. increasing temporal and spatial scales from right to left.

K. Yoshioka (✉)
UFZ, Helmholtz Centre for Environmental Research, Leipzig, Germany
e-mail: keita.yoshioka@ufz.de

M. Nest
IfG, Institut für Gebirgsmechanik, Leipzig, Germany

D. Pötschke
TUBAF, Technische Universität Bergakademie Freiberg, Freiberg, Germany

A. S. Sattari
CAU, Christian-Albrechts-Universität zu Kiel, Kiel, Germany

P. Schmidt · D. Krach
UoS, University of Stuttgart, Stuttgart, Germany

O. Kolditz et al. (eds.), *GeomInt–Mechanical Integrity of Host Rocks*,
Terrestrial Environmental Sciences, https://doi.org/10.1007/978-3-030-61909-1_3

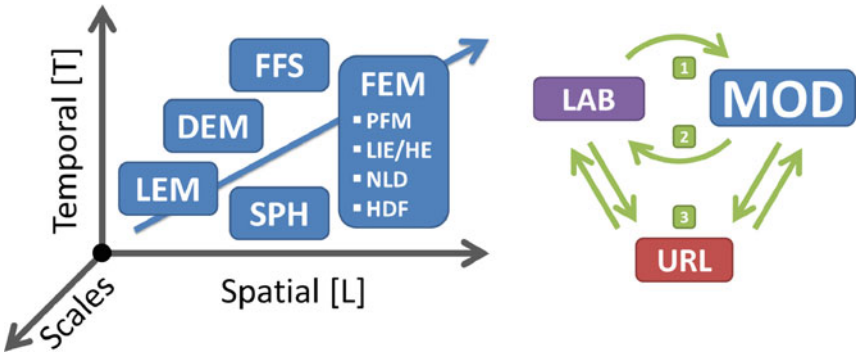

Fig. 3.1 Overview of the Numerical Platform (left) as part of the GeomInt research concept (right), see Sect. 1.2

3.1 State-of-the-Art

3.1.1 THM Simulations and Open Source Development

Process-oriented numerical simulation programmes are necessary for predicting possible environmental impacts as well as for the macroeconomic and safety design of geosystems for underground use with, if necessary, different or even multiple management. These programmes must be able to represent the running processes and their interactions. Already in the mid-eighties of the last century, specific models were developed in the USA and partly implemented in scientific simulation platforms in order to describe THM processes taking place in the geological subsoil which are connected with the thermal use of the subsoil as energy source (geothermics) or energy storage. However, these investigations primarily had a basic character. In addition, the numerical calculation tools are often oriented towards the description of special processes and only partially consider couplings of different physical processes. Geotechnical applications can also be simulated with a number of established commercial program systems. For hydraulic processes such as multiphase flow in porous media are simulators from the oil and gas industry available (e.g. ECLIPSE, STARS), for the description of mechanical processes as well (FLAC3D). All mentioned codes can only cover a part of the necessary process spectrum. Therefore, simulation programs are required which can represent thermal, hydraulic, mechanical, and chemical (THMC) processes coupled, such as TOUGH [78], HYTEC [113], DuMuX [33] or OpenGeoSys [52]. In order to be able to represent the foreseeable impact area of underground use in realistic simulation areas, efforts have been made to parallelise these codes (e.g. OpenGeoSys [125], TOUGH [135]). In particular, the simulation of systems subject to discontinuity requires high performance computing. A major limitation of commercially available numerical simulation programs is that their source codes are not accessible and therefore not transparent and that a

further development of such programs is therefore only possible by the commercial developer. In the research project applied for here, the platforms OpenGeoSys (UFZ (coordinating), BGR, CAU, IfG, TUBAF), mD-LEM (CAU) and pythonSPH (Uni Stuttgart) developed by some of the applicants as open source software can be used, so that the limitations mentioned do not exist. The description of discontinuities with different approaches described in the following as well as their processing in the sense of high-performance computing (HPC) requires targeted program extensions.

3.1.2 Continuum Models (XFEM and Variational Phase Field)

In recent years, extended [10] or also known as generalized [108] finite element methods (XFEM/GFEM) and phase-field methods [14] for the description of existing and developing discontinuities and singularities within continuum mechanical approaches have established themselves ahead of all others. Both methods differ fundamentally and have their own strengths and weaknesses. XFEM locally extends the approach and test function space by formulations that can map the discontinuous course of the solution and introduces corresponding additional local degrees of freedom. Usually, this approach is combined with so-called level set methods, which help to localize the discontinuity and thus ultimately determine in which elements the solution space has to be extended. This approach allows the approximation of discontinuous solutions on comparatively coarse grids, but requires programmatic infra-structures for the treatment of flexible additional degrees of freedom, level sets and other aspects, which require a considerable implementation effort, especially in branched crack systems. In contrast, the variational phase field method was originally proposed as a generalized Griffith criterion by [34] and numerically implemented using a phase-field variable by [15]. In the variational phase-field model, cracks are represented by a smoothly varying function (phase-field variable) that transitions from intact material (phase-field variable = 1.0) to fully broken state (phase-field variable = 0.0) using a regularization parameter with the dimension of a length and the energy consumed by the cracks is computed from this diffused representation. One of the strengths of this approach is to account for arbitrary numbers of pre-existing or propagating cracks in terms of energy minimization, without any a priori assumption on their geometry or restriction on the growth to specific grid directions.

XFEM [10] was originally developed for crack propagation problems and was also applied in the geotechnical context, e.g. for multiphase flows [25, 69] and heat transport [48, 98]. Current developments of generalized and extended finite element methods in the context of hydraulic stimulation are mainly concerned with the efficient coupling of solid-state and flow-mechanical problems [65, 126, 137].

The variational phase-field model of fracture has witnessed wide ranging applicability in from dynamic fracture [13, 17, 56], to ductile fracture [3, 4, 67], to thermal and drying fracture [19, 63, 66]. The first application of the variational phase-field

model to hydraulically driven crack propagation has been proposed by [18] and followed by many others [26, 43, 55, 86, 128, 130] or for land slide modeling [127] with various formulation and numerical implementation. While the reported findings are promising thus far, the method still needs more establishments for practical field scale applications. The required efforts may include validation against laboratory/field experiments, approaches to recover explicit properties such as fluid leak-off from smeared crack representation, and more complex physics phenomena such as visco-elasticity.

3.1.3 Discontinuum Models

Discontinuum models directly map forces of interaction between predefined discrete elements. The latter may themselves be discretized and mapped by continuum mechanics. Decisive for the mapping of developing discontinuities, however, are the pre-defined interfaces subject to certain interface formulations. This type of modelling was applied in geotechnics, for example, to geothermal systems [140] and has also made a decisive contribution to the simulation of the pressure-driven generation of flow paths in polycrystalline salt rocks, which is bound to the discontinuum-mechanical microstructure of the salt rocks [143]. Polycrystalline salt rocks represent a discontinuum of intergrown salt crystals on the micromechanical level [144]. In contrast to porous media, there is no cross-linked pore space in salt rocks. Only by pressure-driven opening and cross-linking of pathways, i.e.g.eneration of connectivity by opening channels along the grain boundaries of the salt crystals, cross-linked flow paths are created in salt rocks. Fluid pressure-driven percolation is direction-dependent and seeks the path of least resistance along the crystal grain boundaries in the polycrystalline salt rock under the effect of the existing stress field [145]. This mechanism of directional percolation can be simulated in coupled HM models on a discontinuity mechanical basis.

The observations on numerical models of pathogenesis by source and shrinkage processes based on a microscale based analysis must be able to map significant structural changes and discontinuity developments in nonisothermal HM coupled processes, which manifest themselves in progressive fracture or self-healing processes under pressure, saturation and temperature influence. First basics of the modelling of fracture processes on the microscale were published at the end of the 1990s with reference to self-organising fracture processes based on Voronoi discretizations [12]. By combining the approaches of HM modelling in saturated media [6] and TM modelling [80], the connection for the simulation of self-organizing fracture processes in geomaterials shall be established with consideration of complex TH^2M processes. Based on the elasticity theory, linear fracture models following Mode I and Mode II were developed for fragile, largely homogeneous material with few inclusions. For materials with high interference, models based on continuum fracture mechanics [110] were developed which require specific information on material microstructure and fracture behaviour. Thermal conductivity in cemented geoma-

terials is determined by heat transfer between mineral particles, porosity, fluid and contact quality [7, 129, 133]. The Thermal Particle Dynamics method can be used to simulate the transient heat propagation in granular media and the associated thermal expansion [115]. This was considered in a thermal DEM [116, 117], but the calculation effort is enormous and the grain or contact shape is greatly simplified [141]. In contrast to the particle methods, the heat propagation in cemented materials can be determined numerically very effectively by classical FEM, but microlevel information disappears due to the underlying homogenization. This poses a problem for the initiation of discontinuities by thermal processes in THM coupling.

The hybrid lattice models have been developed to tackle the shortages in continuum based models, such as the simplicity to define the heterogeneity/anisotropy as well as the fracture simulation and stress redistribution during the frack propagation (discontinuities) without the need to re-mesh the domain [11, 114]. The lattice model is similar to the finite volume (FVM) or finite difference (FDM) methods, with the difference that the FVM or FDM explicitly discretize the continuum [81, 84]. The simplicity and accuracy of lattice models to simulate the fracking in cemented geomaterials, such as rock and concrete [47, 58, 77], are well established. The lattice models in comparison to the continuum methods are time consuming and expensive. Therefore, their applicability and development in real engineering applications or commercial softwares are not well developed. However, with the increase of computational power during past years as well as the implementation of parallel computing or GPU computing methods, the application of lattice models in commercial softwares is imminent.

The mentioned DEM approaches, as classical discontinuum models, have the disadvantage that additional connections between the particles have to be implemented by beam elements, which contain the fracture-mechanical criteria. Lattice based models—LEM [25, 27] have been developed for modeling of fracture mechanical processes considering discontinuity and crack initiation as well as crack propagation. These include a networking of the existing heterogeneity ranges (Voronoi and Delaunay triangulation) and use simple linear fracture criteria on the microscale. The cross-linked two- and three-dimensional continuum regions are microscopically coupled by 1D elements in the center of gravity of the Voronoi cells. In the simplest case these elements are Hookesche springs with a normal stiffness [29]. In three-dimensional space these simple springs already give a good approximation of the Mode I failure model [132]. With the use of Born spring models and an additional tangential degree of freedom, shear behaviour can already be modelled [46]. By extending the spring, for example as a beam element [90], displacements, rotations and moments can be transferred to the node in addition to the forces, whereby an additional bending contact can be taken into account [85]. For the spatial lattice network thus generated, the displacements at each point are determined by generating an equilibrium or by minimizing the energy [64] or dynamic relaxation [28]. The LEM combines the advantages of simple implementation with the ability to control particle interaction in the model while simultaneously self-organizing initiation and progression organization of a discontinuity, [88, 136].

Additionally, in contrast to discrete models, the lattice models can be implemented to represent a continuum, as the lattice elements do not necessarily define the particle to particle contact mechanics [79]. The hybrid lattice model can represent a continuum or particle-to-particle contacts, depending on the objective of the simulation. In both cases, the domain is discretized into series of spring or beam elements, representing the bonds. The regularization of a lattice model grants the independency of the results from the mesh size and meshing technique [75]. The lattice models were initially emerged in order to simulate the fracture initiation and propagation in cemented geomaterials. With the time, lattice models have been extended to simulate the wide variety of the thermal [80, 82, 99], thermo-mechanical [88, 89] and hydro-mechanical [39] problems in the engineering applications. In the recent years, the hybrid lattice models have been extended to determine the granular, cemented or swelling geomaterials response under the coupled thermo-hydro-mechanical (THM) processes.

3.1.4 Smoothed Particle Hydrodynamics

Smoothed Particle Hyrodynamics (SPH) methods are reticule numerical collocation methods for solving partial differential equations. SPH methods were formulated almost 40 years ago to solve astrophysical problems and have been further developed in recent years to solve a variety of problems and models in fluid and solid state mechanics [70]. The SPH method is particularly suitable for problems with free surfaces or material interfaces such as discontinuities and cracks: SPH methods are Updated or Total Lagrange methods, i.e. boundary conditions at discontinuities can be described numerically well. In recent years, great progress has been made in the efficiency of SPH formulations, especially for questions with internal interfaces, such as for non-Darcy flows in porous media or in the multiphase fluidics of immiscible fluids in porous media [73, 112]. The so-called "Whole Domain Formulation", i.e. a numerical procedure in which the surface conservation equations (mass and momentum), such as the Young-Laplace equation in multiphase fluidics, are "smeared" by means of the kernel function and integrated into the bulk conservation equations (Continuum Surface Force—CSF), can be interpreted here as a "phase field method" which "continuously smears" the physical properties of the discontinuities. Besides the consideration of the SPH-inherent kernel function in the CSF methods and the absence of the need to artificially adduce discontinuities, the net-free SPH methods above all show great efficiency advantages when complex and small-scale (pore) geometries are to be precisely mapped [101]. In addition to small-scale direct numerical simulations on the pore space scale, SPH methods for coupled HM problems in geomechanics have already been developed [20, 21]. The two HM-coupled biotubes poroelastic equation sets for the porous solid phase and the viscous pore fluid were formulated in these works with two disjunctive particle sets which can lead to difficulties in impulse interaction modelling. A further development of the SPH method for HM processes, also taking into account propagating

discontinuities such as cracks and crack networks, is therefore imperative to establish the SPH method as an efficient and reliable tool for geoscientific problems.

All the approaches described above have proved to be suitable in principle for the physical analysis of the growth of discontinuities. However, in connection with the extension of the methods to coupled THM processes, there is still a fundamental need for development in many areas. This is to be supported by an improved process understanding to be worked out, by building on it some of the numerical methods used here are to be further developed purposefully beyond the state of the art. Applications that go beyond the simulation of laboratory experiments and use the methods for solving practically motivated problems of large-scale geosystems have so far hardly been found in the literature or have not even been developed for certain essential process couplings. There is an urgent need for systematic investigations into the questions of how these methods can be translated into practical applications, what computing resources are required, and in which cases certain methods appear more suitable than others. The aim of this project is to develop such an overall view and a systematic comparison of the methods at defined benchmarks as well as their embedding in proven software, partly with the inclusion of methods of high performance computing.

3.2 Numerical Methods

3.2.1 FFS—Forces on Fracture Surfaces

This numerical method explicitly uses the geometry of a rock surface and calculations on single surface elements are executed. The main advantage of this method is the possibility to closely look inside the mechanisms which control the shear behaviour of the joint (Fig. 3.2). The drawback is the high computation time needed due to the more complex calculation scheme.

Starting point were the works by [23, 31]. The last mentioned work uses a FFS approach. The geometry of surface is represented as a triangular surface. The apparent dip angles θ^* for the elements are calculated. An iterative scheme decides whether the surface can slide over its counterpart or whether the surface elements in contact

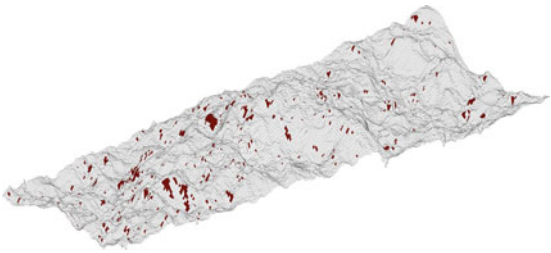

Fig. 3.2 The elements used in a shear test simulation are marked in red. The FFS approach is able to look directly inside a model and helps to deepen the understanding of the active processes

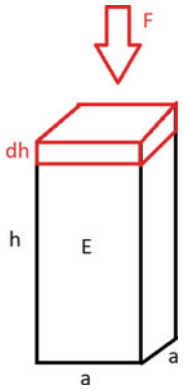

Fig. 3.3 A surface element is represented as a rock column which withstands normal forces by elastic deformation

are destroyed. In the case of destruction the geometry is corrected and the next check for sliding versus destruction starts. The two important formulas are the one for the sliding forces:

$$F_{\text{slide}} = F_{\text{loc}} \tan(\varphi_b + \theta^*) \tag{3.1}$$

where F_{loc} is the local force acting on one element, φ_b is the basic friction and θ^* the apparent dip angle of this element. The other formula is the one for shear forces, which is the force needed to destroy the surface element:

$$F_{\text{shear}} = A \ (c + \sigma_{\text{loc}} \tan(\Phi)) \tag{3.2}$$

where A is the ground area of the element, c the cohesion of the rock material, σ_{loc} the local normal stress and Φ the angle of inner friction of the rock material.

The idea of the newly developed approach is to have a physically consistent calculation scheme. Therefore the normal forces of the surface elements in contact have to be estimated. The simplest approach was chosen to keep things manageable. An elastic stress-displacement behaviour was basically used (Fig. 3.3). The resulting formula is:

$$F_n = \sum_i \left(E\, a^2 \, \frac{\Delta h_i}{h} \right) \tag{3.3}$$

For all i surface elements in contact the relative height change $\frac{\Delta h_i}{h}$, the ground area a^2 and the Young's modulus E were used. For a specific rock joint the two surfaces are moved towards each other until the force created by the elastic deformation equals the force which is applied to the fracture. Another simplification compared to [23] is the usage of quadratic grid elements. This allows to store the height values in a matrix form which is easy to handle.

3.2.2 LEM—Lattice-Element-Method

The application of the lattice element in modeling the fracture initiation and propagation in geomaterials has been well established [58, 77, 114]. The main advantage of the LEM over other numerical methods is the ability to model the stress redistribution and concentration upon the fracking process. The application of the LEM is extended to model the heat transfer in cemented geomaterials [89] as well as non-cohesive granular particles [83]. The thermo-mechanical lattice model based on the integration of the interface element is able to model the expansion and shrinkage processes during the heating and cooling cycles [88]. The LEM is also implemented to model the foam concrete behavior under dynamic loading [81]. In the past decade, using the dual lattice model to simulate the coupled hydro-mechanical loadings in geomaterials has developed [39]. In these models, the dual mesh grid for the fluid transport is generated. The short description of the implemented coupled thermo-hydro-mechanical lattice method is given below.

Discretization of the Domain

The domain is discretized into a series of Voronoi cells to represent the individual particles or a continuum depending on the purpose of the investigation. With the application of the vectorized random lattice (VRL), the irregularity factor known as the randomness factor (α_R), which varies between 0 and 1, is introduced [74]. When the randomness factor is 0, the generated mesh is regular and when it is equal to 1, it reaches the maximum irregularity for VRL model. Afterward, the Voronoi tessellation is implemented and polygonal cells are generated (see Fig. 3.4a, b). The Delaunay triangulation process results in the Voronoi cell connectivity, which are defined as the bond elements between two adjacent nodes.

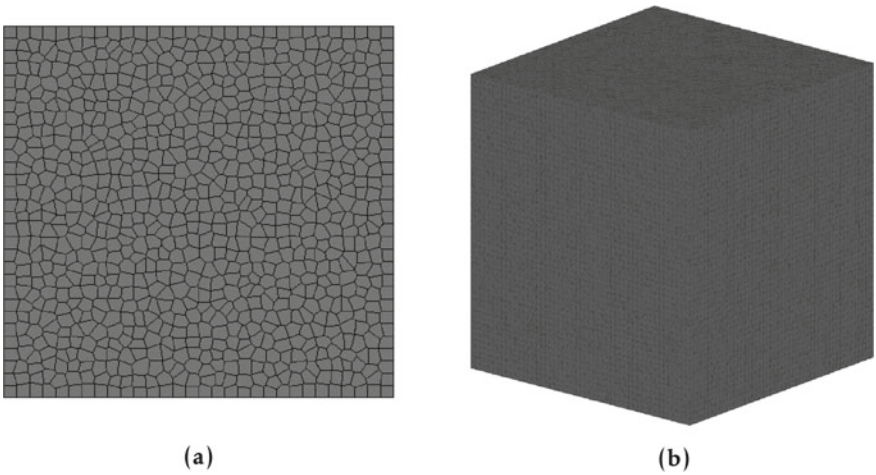

Fig. 3.4 The generated domain with $\alpha_R = 0.5$. **a** 2D discretization, and **b** 3D discretization

Mechanical Lattice Model

The mechanical lattice model is based on the assumption of the Mode I and II linear elastic fracture mechanics. The simulation of the fracture in LEM is based on the removal of the bond elements between the neighboring Voronoi cells [79]. The elements strength threshold is defined based on the critical strain energy or the fracture toughness for Mode I and II. In a different approach, the strength threshold is defined based on the Mohr-Coulomb's tension cutoff model [11]. The lattice elements are represented by a series of spring (1DOF), Euler-Bernoulli beam (3DOF) (Fig. 3.5) or Timoshenko beam elements (4DOF). The regularization of the regular lattice model, such as a triangular or square discretization technique, is carried out and a relationship between the continuum and element properties is presented [47, 75]. This regularization assumes that the stored strain energy of a continuum, $U_{\mathbb{R}}$, is equal to the stored strain energies in each individual Voronoi cells, U_{Cell}. The strain energy stored in a unit cell depends on the total number of each cells bond elements (N_b), the elements response forces (F_b) and the response displacements (u_b). For a continuum, the stored energy depends on the continuum stresses ($\sigma_{\mathbb{R}}$) and continuum strains ($\varepsilon_{\mathbb{R}}$) throughout the continuum volume ($V_{\mathbb{R}}$).

$$U_{\text{cell}} = U_{\mathbb{R}} \tag{3.4}$$

$$U_{\text{cell}} = \frac{1}{2} \sum_{b=1}^{b=N_b} F_b \, u_b \tag{3.5}$$

$$U_{\mathbb{R}} = \frac{1}{2} \int_{V_{\mathbb{R}}} \sigma_{\mathbb{R}} \, \varepsilon_{\mathbb{R}} \, dV \tag{3.6}$$

For a discretized 2D domain with the spring element, the length of the element (L_b), alignment orientation ($n_{i,j,k,m}$), first stiffness coefficient ($(R)'$), continuum stiffness matrix $C_{\mathbb{R}}$, and strains of $\varepsilon_{i,j,k,m}$ are correlated as,

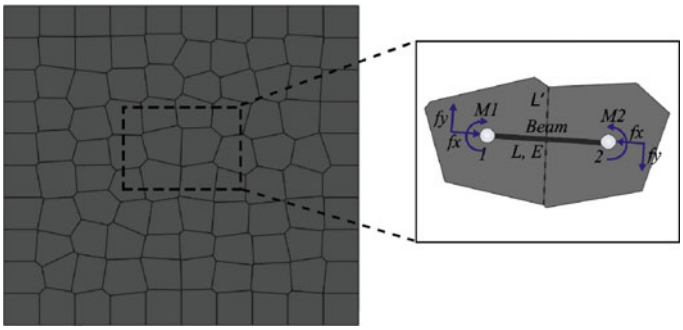

Fig. 3.5 The Euler-Bernoulli beam element representing the bond between two cells

$$U_{\text{cell}} = \frac{1}{2} \sum_{b=1}^{b=N_b} L_b^2 \left((R)' \, n_i \, n_j \, n_k \, n_m \, \varepsilon_{ij} \, \varepsilon_{km} \right)_b \tag{3.7}$$

$$U_{\mathbb{R}} = \frac{1}{2} \varepsilon_{\mathbb{R}} \, C_{\mathbb{R}} \, \varepsilon_{\mathbb{R}} \tag{3.8}$$

For a Euler-Bernoulli beam element in 2D, the curvature strain ($\kappa_{i,j}$), curvature stiffness ($D_{i,j}$), stiffens matrix ($C_{i,j,k,m}$) and second stiffness coefficient ($(R)''$) are related as,

$$U_{\mathbb{R}} = \frac{V}{2} \varepsilon_{ij} C_{ijkm} \varepsilon_{km} + \frac{V}{2} \kappa_i D_{ij} \kappa_j \tag{3.9}$$

$$C_{ijkm} = \sum_{b=1}^{b=N_b} \left(n_i \, n_k \left(n_j \, n_m \, (R)' \right) + n_j \, n_m \, (R)'' \right)_b \tag{3.10}$$

After the regularization of the lattice model and with the minimization of the potential energy of the system, the load versus displacement relation in each time step is determined. For a single element, the stored total strain energy (U_t^b) is equal to the sum of axial (U_a^b), shear (U_s^b) and moment (U_m^b) strain energies. Eventually, the total strain energy depends on the axial force (f_x), shear force (f_y) and moment (M_b) along the element's length of $z = 0 : L_b$, the area of elements (A_b), element's shear modulus (G_b), element's Young's modulus (E_b), and moment of inertia (I_b). The bi-linear softening scheme is implemented to model the quasi-brittle material behavior existing in rock and concrete geomaterials [45]. The measured E_b values depends on the peak strain (ε_p), failure strain (ε_f), current element strain (ε_b) and peak load (f_p) where the stiffness degradation starts.

$$U_t^b(z) = U_a^b(z) + U_s^b(z) + U_m^b(z) = \frac{1}{2} \int_0^{L_b} \left(\frac{f_x(z)^2}{E_b A_b} + \frac{f_y(z)^2}{G_b A_b} + \frac{M_b(z)^2}{E_b I_b} \right) \cdot dz \tag{3.11}$$

$$E_b = \frac{f_p}{\varepsilon_f - \varepsilon_p} \left(\frac{\varepsilon_f}{\varepsilon_b} - 1 \right) \tag{3.12}$$

Thermo-mechanical Lattice Model

The thermo-mechanical lattice model is based on the weak coupling scheme between the thermal and mechanical models, which decreases the computational costs. The thermal lattice model is based on the discrete thermal lattice model (TDEM) [32, 142], where the Hertzian contact model is implemented to account for the heat conductance (h_b) between the particles. The axial compression force increment (f_x)

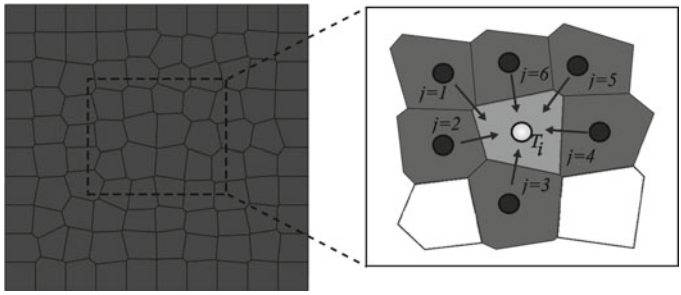

Fig. 3.6 The heat flow into i_{th} cell from surrounding boundaries

results in higher thermal conductance between the particles, which eventually leads to a higher effective thermal conductivity (K_{eff}). The regularization of the thermal lattice model is based on the relationship between the heat conductivity of elements and the continuum [83]. The h_b depends on the contact length (L_b') (or area in 3D domain), contact forces and assigned elements thermal conductivities (k_b).

$$h_b = k_b \left((L_b') + \left(\frac{3 f_x L_b}{4 E_b} \right)^{\frac{1}{3}} \right) \tag{3.13}$$

In a steady state, the amount of the heat in- and outflow (q_b) from a Voronoi cell (Fig. 3.6) is equal to zero,

$$\rho_i c_i v_i \frac{dT_i}{dt} - \nabla \cdot (k_i \nabla T_i) - \rho_i \dot{q}_i = 0 \tag{3.14}$$

$$\nabla \cdot (k \nabla T_i) = \sum_{b=1}^{b=N_b} q_b = \sum_{b=1}^{b=N_b} h_b (T_i - T_j)_b = 0 \tag{3.15}$$

where, $\dot{q}$ is heat density (assumption: $\dot{q} = 0$), t is time, ρ_i is density, c_i is heat capacity and v_i is the volume of each Voronoi cell (i). In a transient case,

$$\sum_{b=1}^{b=N_b} q_b = \rho_i c_i v_i \frac{dT_i}{dt} \tag{3.16}$$

The effective thermal conductivity is calculated based on the average volume technique, where q_{ave} is the average heat flow, q_{Cell}^b is the heat flow through the assigned cells located in the boundary (N_C), $\dot{T}$ is the temperature gradient and $\hat{x}_{cell}$ is the relative coordinates of each cell.

$$q_{ave} = \frac{\sum_{b=1}^{b=N_C} q_{Cell}^b \cdot \hat{x}_{Cell}}{V} \tag{3.17}$$

$$q_{ave} = K_{eff} \cdot \dot{T} \tag{3.18}$$

The thermal strain is calculated based on the linear expansion of the lattice elements and the given heat expansion coefficient. The implementation of the thermal expansion into the mechanical model results in a fully coupled thermo-mechanical model [88].

Hydro-mechanical Lattice Model

The existing hydro-mechanical lattice models are based on the assumption of the dual lattice network, where the mechanical lattice elements transfer the mechanical loads between the two nodes and the conduct elements perpendicular to the alignment of the mechanical elements transfer the fluid or gas flow between the conduct nodes [39, 40]. The implemented hydro-mechanical lattice model is based on the mass conservation (m_f) of the fluids in the continuum. The hydraulic aperture (a_h), fluid density (ρ_f), fluid viscosity (ν_f), flow length (L'_b), hydraulic resistance (R_h), saturation degree (Sr) and bulk modulus (K_f) are the main parameters used to determine the hydraulic pressures (P_f) and transferred fluid masses (Δm_f) between the conduct nodes.

$$m_f^{t+1} = m_f^t + \Delta m_f \tag{3.19}$$

$$m_f^{t=0} = \mathrm{Sr}^{t=0} V_{cav} \rho_f \left(1 + \frac{P_f^{t=0}}{K_f}\right) \tag{3.20}$$

$$\Delta m_{f,ij} = f(Sr) \frac{P_{f,j} - P_{f,i} - \rho_f g \left(Z_j - Z_i\right)}{R_h} \Delta t \tag{3.21}$$

where, Z is the relative coordinate of the i, j conduct nodes, V_{cav} is the volume of the cavity, g is the gravity and $f(Sr)$ is the saturation function which is equal to 0 and 1 in a dry and saturated conditions, respectively. According to the finite-discrete element method (FDEM) [57], the fluid mass is stored within defined physical and artificial cavities. Each conduct node represents an artificial cavity connected through conductive elements (Fig. 3.7), where the hydraulic conductivity is governed based on the parallel plate cubic flow rule.

$$R_h = \frac{12\nu_f}{a_h^3} L'_b = 12\nu_f \int_{z_i}^{z_j} \frac{1}{a_h(z^3)} dz = \frac{6\nu_f (a_{h,j} + a_{h,i})}{(a_{h,i} a_{h,j})^2} L'_b \tag{3.22}$$

When an artificial cavity is saturated, the amount of excessive fluid mass flowing inside the cavity builds the pore pressure, which then is transmitted into the mechanical nodes. If the cavity is not saturated, then the pore pressure is assumed to be zero.

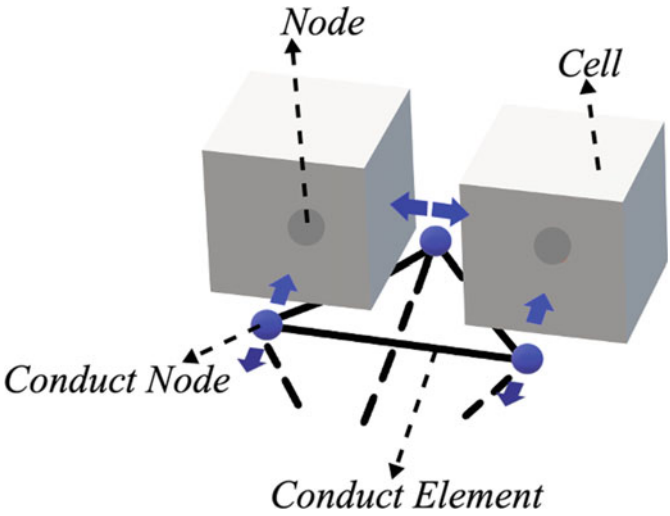

Fig. 3.7 The schematic representation of the implemented hydro-mechanical model

$$P_f^t = P_f^{t-1} + K_f \frac{\Delta m_f}{\rho_f V_{\text{cav}}^t} \quad \text{if} \quad \text{Sr}^t = 1 \tag{3.23}$$

With the implementation of the pore pressures into the mechanical lattice nodes, the pore pressure diffusion and the change of the hydraulic conductivity with the crack opening and closure are measured. The flow simulation is implemented under both the pressure- and flowrate-controlled boundary conditions.

Shrinkage and Swelling Lattice Model

The simulation of the shrinkage and swelling using the lattice element method is based on the particle shrinkage model [100], which is mainly considered in the discrete models. In contrast to the DEM, the shrinkage in LEM is implemented into the lattice elements (Fig. 3.8). To do so, the interface elements are generated to represent the bond between the particles [88]. The shrinkage and swelling coefficients (α_s) are temperature dependent. According to the initial water content ($\omega^{t=0}$) and the change of the water content during the shrinkage and swelling process, the linear strain in the lattice elements is determined and implemented into the mechanical model.

$$L_b^t = L_b^{t=0} e^{-\alpha_s \cdot \frac{t}{t=\infty}} \tag{3.24}$$

$$\alpha_s = -\frac{1}{3} \ln \left(1 - \frac{\omega^{t=0} - \omega^t}{1 + e_0} \cdot G_s \right) \tag{3.25}$$

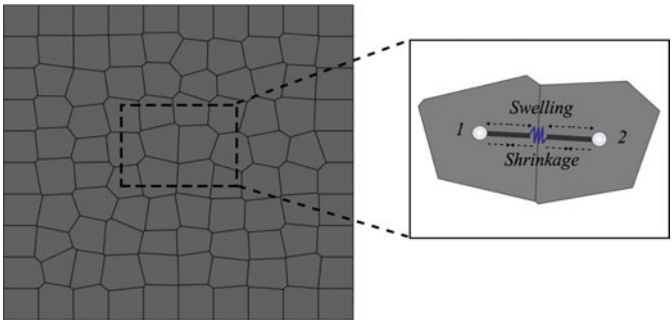

Fig. 3.8 The implementation of the interface element to simulate the shrinkage and swelling processes

The shrinkage and swelling coefficient are time, temperature and depth dependent. Therefore, graphs representing the evaporation rate as well as the soil water characteristic curves to assess the applied suction and the water content during the wetting and drying paths are required [124]. $\bar{\bar{\sigma}}$ and $\bar{\bar{\varepsilon}}$ are the stress and strain tensors, respectively.

$$\bar{\bar{\sigma}} = C : \bar{\bar{\varepsilon}} - \mathrm{Sr}\, P_f \bar{\bar{\delta}} \tag{3.26}$$

The elements shrinkage and expansion results in the axial compression and tensile stresses in the lattice elements, which when they exceed their predefined strength threshold are removed, is simulated as well as the micro fracking process under shrinkage and swelling conditions.

3.2.3 DEM—Distinct-Element-Method

The distinct element method (DEM) extends the capabilities of continuum-mechanical approaches by introducing a new level of discretization, which allows it to describe independent deformable bodies that can interact via their contact points and surfaces, see Fig. 3.9. The behaviour of these contacts can be modelled using joint constitutive models, which are typically formulated in terms increments. This approach is especially suitable for materials with a pronounced grain structure, such as salt rocks.

The models of rock salt, from laboratory scale samples to entire potash mines, therefore need to be built from randomised assemblies of polyhedral grains, in order to simulate the discontinuous and granular nature. The generation of the randomised structures is based on Voronoi-discretization, which allows to divide arbitrary volumes (areas) into polyhedral parts. The program generates pseudo-random point clouds using a Monte-Carlo-method, which can then be refined to avoid clustering.

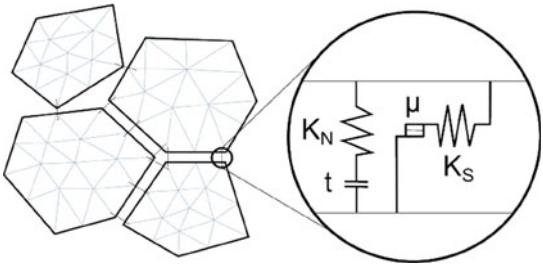

Fig. 3.9 Interaction between blocks and contacts in the DEM

It is also possible to introduce a local variation of the grains size this way. The thermo-hydro-mechanical behaviour of a model set up in this way is then a combination of the behaviour of the of bulk of the grains, and of the contact properties. For both, constitutive laws were derived at IfG [146].

Since it would be computationally unfeasible to represent a large geological structure with realistic grain sizes of millimeters or centimeters, a coarse-grained approach is taken. This approach was validated by carrying out discretization studies with a variation of Voronoi sizes. The blocks/grains dominate the hardening and the creep behaviour, while the softening occurs predominantly by shear and tensile failure on grain boundaries [147].

Another advantage of the discontinuum mechanical approach lies in its capabilities to model the pressure driven percolation of gases and fluids on discrete flow paths on opened grain boundaries. The undamaged grain boundaries start out as impermeable but can be opened due to plastic failure.

The constitutive laws for both bulk and contacts were implemented as DLLs for the programs UDEC and 3DEC of Itasca CG, Inc.

3.2.4 SPH—Smoothed-Particle-Hydrodynamics

Direct Numerical Simulations (DNS) of effective physical properties of single-phase flow through porous or fractured solid materials can be performed directly on the pore scale of the porous soil or rock. Morphological information, the basis for the subsequent DNS, is obtained as segmented (binarized) voxel-data from μ X-Ray Computed Tomography (XRCT). In general, numerical simulations of flow processes on XRCT-data at small to moderate Reynolds (Re) numbers could be performed by mesh-based Finite Element, Finite Differences or Finite Volume methods.

Here, we haven chosen the mesh-less Smoothed Particle Hydrodynamics methods as an alternative simulation technique. SPH is a Lagrangian simulation tool used to solve Partial Differential Equations (PDE) and was originally developed for astrophysical problems [36, 59]. In recent years, due to it's flexibility and scalability and applicability on HPC architectures, especially in an explicit formulation, it became attractive for various problems fluid dynamics like single and multi-phase

fluid mechanics with internal interfaces, suspension flow, and single and multi-phase flow in porous media [61, 102–105].

Within the framework of this method, the discretisation of the PDEs spans a set of interacting collocation points $\mathcal{P}_i$ with position vectors $\mathbf{x}_i$, referred to as particles. The positions of the particles represent integration points at which field functions $\Phi(\mathbf{x}, t)$ are interpolated by convolution with the Dirac-Delta function δ:

$$\Phi(\mathbf{x}, t) = \int_{\Omega} \Phi(\mathbf{x}', t)\, \delta(\mathbf{x} - \mathbf{x}')\, \mathrm{d}v. \tag{3.27}$$

Replacing $\delta(\mathbf{x} - \mathbf{x}')$ with the kernel function $W(\mathbf{x} - \mathbf{x}', h)$ results in the approximation

$$\Phi(\mathbf{x}, t) \approx \int_{\Omega} \Phi(\mathbf{x}', t)\, W(\mathbf{x} - \mathbf{x}', h)\, \mathrm{d}v, \tag{3.28}$$

where the support h of the kernel determines a sphere of influence and likewise declares neighbouring particles $\mathcal{P}_j$ with position vector $\mathbf{x}_j$. Subsequently, the discretisation (numerical integration) of the integral formulation converts continuous field functions into discrete particle properties $\Phi(\mathbf{x}_i) = \Phi_i$, kernel representations into spatial discretisation and Eq. (3.28) yields

$$\Phi_i = \sum_{j}^{N} \Phi_j\, W(\mathbf{x}_i - \mathbf{x}_j, h)\, V_j. \tag{3.29}$$

Herein, V_j is introduced as the discrete representation of $\mathrm{d}v$ and $j = 1, 2, \ldots, N$ indicates the neighbour particles within the kernel support of particle $\mathcal{P}_i$. Analogously, differential operators turn into short-range interaction forces. For more technical details, also accounting to the necessary time integration we refer to [72, 103, 138].

3.2.4.1 Single-Phase Flow of a Newtonian Fluid

A SPH implementation of single-phase flow of a Newtonian fluid is based on the solution of the balance of momentum in the present local form

$$\rho^{\mathrm{f}}\, \dot{\mathbf{v}}_{\mathrm{f}} = \mu^{\mathrm{f}}\, \mathrm{div}\, (\,\mathrm{grad}\, \mathbf{v}_{\mathrm{f}}) - \mathrm{grad}\, p + \rho^{\mathrm{f}}\, \mathbf{b} \tag{3.30}$$

and the balance of mass

$$\dot{\rho}^{\mathrm{f}} = -\rho^{\mathrm{f}}\, \mathrm{div}\, \mathbf{v}_{\mathrm{f}}, \tag{3.31}$$

which are known as the Navier-Stokes equations. We adopted the notation used in mixture theory [106, 107] where a subscript is used for kinematic quantities and a superscript elsewhere. $\rho^{\mathrm{f}}(\mathbf{x}, t)$ is the mass density field, $\mathbf{v}_{\mathrm{f}}$ is the velocity vector, μ^{f}

is the dynamic viscosity, $p(\mathbf{x}, t)$ is the pressure field and $\mathbf{b}$ are body force densities. The "dot" operator, cf. Eqs. (3.30) and (3.31), is denoting the material or substantial time derivative $\cdot(\bullet) = \partial_t \bullet + \text{grad}\,(\bullet) \cdot \mathbf{v}_\mathrm{f}$. In order to solve the quasi-incompressible (weakly compressible) character of the Navier-Stokes equations an equation of state for the pressure in the form $p(\rho^\mathrm{f})$ has to be formulated. Therefore, either a linear model or the Tait equation [42]

$$p(\rho^\mathrm{f}) = \frac{\rho_0^\mathrm{f} c_\mathrm{f}^2}{\gamma}\left[\left(\frac{\rho^\mathrm{f}}{\rho_0^\mathrm{f}}\right)^\gamma - 1\right] \tag{3.32}$$

is commonly employed, wherein $c_\mathrm{f} = \sqrt{K^\mathrm{f}/\rho^\mathrm{f}}$ is the speed of sound of the fluid with the bulk modulus K^f and γ is a constant, specific to the modeled problem (usual $\gamma = 7$ for quasi-incompressible fluids).

3.2.4.2 Discrete Equations

By applying the above introduced transformation from continuous field equations to discrete algebraic SPH equations, the total force on each fluid particle $\mathcal{P}_i$ is obtained as the sum of the discrete body forces $\mathbf{F}_i^B = m_i\,\mathbf{b}$, viscous interaction forces $\mathbf{F}_{ij}^V$ and pressure interaction forces $\mathbf{F}_{ij}^P$

$$m_i \dot{\mathbf{v}}_i = \sum_j^N \mathbf{F}_{ij}^P + \sum_j^N \mathbf{F}_{ij}^V + \sum_j^N \mathbf{F}^B, \tag{3.33}$$

which leads to a relation for the particle velocity update

$$\dot{\mathbf{v}}_i = -\sum_j^N m_j \left(\frac{p_i}{{\rho_i}^2} + \frac{p_j}{{\rho_j}^2}\right)\frac{\mathbf{x}_{ij}}{r_{ij}}\frac{\partial W_{ij}}{\partial r_{ij}} \tag{3.34}$$

$$+ \sum_j^N \frac{m_j(\mu_i + \mu_j)(\mathbf{v}_i - \mathbf{v}_j)}{\rho_i \rho_j}\left(\frac{1}{r_{ij}}\frac{\partial W_{ij}}{\partial r_{ij}}\right) + \mathbf{b}. \tag{3.35}$$

Reconfiguration of the balance of mass, cf. Eq. (3.31) yields

$$\dot{\rho}_i = \sum_j^N m_j(\mathbf{v}_i - \mathbf{v}_j) \cdot \frac{\mathbf{x}_{ij}}{r_{ij}}\frac{\partial W_{ij}}{\partial r_{ij}}. \tag{3.36}$$

However, the density field can also be calculated by an accumulative kernel interpolation $\rho_i = \sum m_j W_{ij}$.

3.2.4.3 Boundary Conditions, Time Integration and Artificial Viscosity

For the application of single-phase flow though porous media, the solid skeleton is considered to be rigid and fluid-solid interfaces Γ^{FS} generally satisfy no-slip and no-penetration boundary conditions. More general solid-fluid interaction phenomena could be considered in SPH formulations, e.g. to mimic rough rock surfaces with asperities, but are not further discussed in the following. To that end, the solid domain is populated by so-called "dummy" particles [103, 138]. The velocity and pressure of these dummy particles is extrapolated by the fluid phase and computed by the balance of momentum, respectively, following the method proposed by Adami et al. [1]. Resulting velocity and pressure fields of dummy particles are counteracting those of the fluid phase and thus create no-slip and no-penetration conditions on Γ^{FS}. The discrete particle properties are updated by the Velocity Verlet time integration method [109, 119] which is a common time-integration scheme in particle methods. Further, a dissipative artificial viscosity term is used to reduce non-physical oscillations, e.g. [71, 72, 138].

FEM—Finite-Element-Method

Figure 3.10 shows a conceptual illustration of three different approaches for modeling displacement discontinuities: (a) cohesive zone model using lower-dimensional (i.e. co-dimension 1) interface elements with local enrichment to represent a strong displacement discontinuity (see Sect. 3.2.4.3); (b) phase-field models of brittle fracture in which a crack surface density per unit volume is introduced for regularisation (see Sect. 3.2.5); and (c) non-local elasto-plastic damage models, in which a kernel function with a specified support region is used to characterize a fracture process zone. In the latter two approaches the discontinuities are smeared over a zone characterized by a length-scale parameter. All models (a–c) are implemented in OpenGeoSys.

In the following we briefly introduce two of the Finite-Element-Method based approaches. The first approach is the variational phase-field implemented in Open-

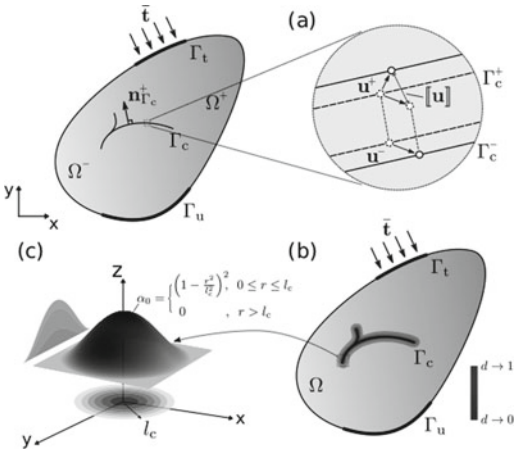

Fig. 3.10 Smeared and explicit numerical representations of fracture. Figure reproduced from [139]

GeoSys and is particularly suited for simulaiton of fracturing process. The second is the hybrid dimensional formulation and is specifically designed for numerical stable fractured-porous media analysis.

3.2.5 PFM—Variational Phase-Field Method

Phase-field models have become one of the most established numerical techniques for fracturing simulation in the last two decades. The approach was first introduced by Bourdin et al. [15] as a numerical implementation method to the variational approach to fractures proposed by Francfort and Marigo [34]. Since the initial inception of the method, models for brittle and cohesive fracture have been further studied by many others [4, 5, 16, 41, 53, 60, 76, 87, 111, 118, 120, 134] including advanced numerical solution schemes [30, 35]. Lately, its application ranges from ductile fracturing [3, 4, 54, 66] to fatigue [2, 96], desiccation fracture [22, 63], and dynamic fracturing [13, 17, 44, 56, 91].

Regularisation of the Total Energy Functional

In the variational approach to fractures in [34], the total energy in the system is defined as the sum of the elastic strain energy, the potential of the external forces and the surface energy as:

$$E(\mathbf{u}, \Gamma_c) := \int_{\Omega \setminus \Gamma_c} \psi(\mathbf{u}) \, \mathrm{d}\Omega - \int_{\partial_N \Omega} \bar{\mathbf{t}} \cdot \mathbf{u} \, \mathrm{d}\Gamma - \int_{\Omega \setminus \Gamma_c} \varrho \mathbf{b} \cdot \mathbf{u} \, \mathrm{d}\Omega + G_c \int_{\Gamma_c} \mathrm{d}\Gamma, \tag{3.37}$$

where ψ is the strain energy density, $\bar{\mathbf{t}}$ is the boundary traction force, $\mathbf{u}$ is the displacement, ϱ is the mass density of the porous medium, $\mathbf{b}$ is the applied specific body force, and G_c is the critical energy release rate. For hydraulic fracturing, the work done by the fluid pressure within the fracture p needs to be added to the energy, and the total energy becomes:

$$\begin{aligned} E(\mathbf{u}, \Gamma_c) := & \int_{\Omega \setminus \Gamma_c} \psi(\mathbf{u}) \, \mathrm{d}\Omega - \int_{\partial_N \Omega} \bar{\mathbf{t}} \cdot \mathbf{u} \, \mathrm{d}\Gamma - \int_{\Omega \setminus \Gamma_c} \varrho \mathbf{b} \cdot \mathbf{u} \, \mathrm{d}\Omega + G_c \int_{\Gamma_c} \mathrm{d}\Gamma \\ & + \int_{\Gamma_c} p[\![\mathbf{u}]\!] \cdot \mathbf{n}_\Gamma \, \mathrm{d}\Gamma \end{aligned} \tag{3.38}$$

where $\mathbf{n}_\Gamma$ is the normal direction to the crack set Γ. Following Bourdin et al. [18], with introduction of a phase-field order variable (or damage variable) d (3.38) is regularised as:

$$E(\mathbf{u}, d, p) = \int_{\Omega} (1-d)^2 \psi(\mathbf{u}) \mathrm{d}\Omega - \int_{\partial_{\mathrm{N}}\Omega} \bar{\mathbf{t}} \cdot \mathbf{u} \, \mathbf{ds} - \int_{\Omega} \varrho \mathbf{b} \cdot \mathbf{u} \, \mathrm{d}\Omega + \frac{G_{\mathrm{c}}}{4 c_w} \int_{\Omega} \left(\frac{w(d)}{\ell} + \ell \, |\nabla d|^2 \right) \mathrm{d}\Omega + \int_{\Omega} p \mathbf{u} \cdot \nabla d \, \mathrm{d}\Omega. \tag{3.39}$$

where d is the damage variable that equals 0 when undamaged and 1 for a fully damaged state, c_w is a normalization parameter defined as $c_w := \int_0^1 \sqrt{w(s)} \mathrm{d}s$, ℓ is a regularisation length, and $w(d)$ is the dissipative energy function. Various possible dissipative energy functions $w(d)$ are discussed in [60]. The most widely used function is a quadratic form [15, 51, 53, 68] $w(d) = d^2$. The variational phase-field model with this choice of the dissipative function is called $\mathtt{AT}_2$ model in [19], and we follow this terminology in this report. Another choice for $w(d)$ is a linear form $w(d) = d$ and is known as $\mathtt{AT}_1$. A thorough study comparing these two models in terms of fracture nucleation and propagation can be found in [111]. Note that in arriving at (3.39), the work done by the fracture pressure in the crack is approximated as $\int_{\Omega} p \mathbf{u} \cdot \nabla d \, \mathrm{d}\Omega$.

Numerical Implementation

The solution of (3.39) follows the alternate minimisation scheme introduced in [15] with respect to $\mathbf{u}$ and d given a time-evolving p. Thus, the minimisation problem can be stated as

$$(\mathbf{u}, d)^* = \underset{\begin{cases} \mathbf{u} \in H^1 \\ d \in H^1, d^t \subset d^{t+\Delta t} \end{cases}}{\arg \min} \tilde{E}(\mathbf{u}, d, p) \ , \tag{3.40}$$

The first variation of the energy functional with respect to $\mathbf{u}$ is

$$\delta E(\mathbf{u}, d, p; \delta \mathbf{u}) = \frac{1}{2} \int_{\Omega} (1-d)^2 \mathbf{C}(\mathbf{u})) : \boldsymbol{\epsilon}(\delta \mathbf{u}) \, \mathrm{d}\Omega - \tag{3.41}$$

$$- \int_{\partial_{\mathrm{N}}\Omega} \mathbf{t} \cdot \delta \mathbf{u} \, \mathrm{d}\Gamma - \int_{\Omega} \varrho \mathbf{b} \cdot \delta \mathbf{u} \, \mathrm{d}\Omega + \int_{\Omega} p \delta \mathbf{u} \cdot \nabla d \, \mathrm{d}\Omega, \tag{3.42}$$

where $\mathbf{C}$ is the constitutive relation that satisfies $\psi = \mathbf{C}(\boldsymbol{\epsilon}) : \boldsymbol{\epsilon}/2$. The first variation of the energy functional with respect to d of $\mathtt{AT}_1$ is:

$$\delta E(\mathbf{u}, d, p; \delta d) = - \int_{\Omega} d \delta d \mathbf{C}(\boldsymbol{\epsilon}(\mathbf{u})) : \boldsymbol{\epsilon}(\mathbf{u}) \mathrm{d}\Omega + \frac{3 G_{\mathrm{c}}}{8} \int_{\Omega} \left(\frac{\delta d}{\ell} + 2 \ell \nabla d \cdot \nabla \delta d \right) \mathrm{d}\Omega + \int_{\Omega} p \mathbf{u} \cdot \nabla \delta d \, \mathrm{d}\Omega, \tag{3.43}$$

and $\mathtt{AT}_2$ is

$$\delta E(\mathbf{u}, d, p; \delta d) = -\int_\Omega d\delta d \mathbf{C}(\boldsymbol{\epsilon}(\mathbf{u})) : \boldsymbol{\epsilon}(\mathbf{u}) \mathrm{d}\Omega + G_\mathrm{c} \int_\Omega \left(\frac{d}{\ell} \delta d + \ell \nabla d \cdot \nabla \delta d \right) \mathrm{d}\Omega + \int_\Omega p\mathbf{u} \cdot \nabla \delta d \, \mathrm{d}\Omega. \tag{3.44}$$

It should be noted that the solution of (3.43) or (3.44) for d is not bounded in $[1, 0]$. Therefore, the solution scheme would require enforcement of the variational inequality ($0 \leq d \leq 1$). For this study, a variational inequality non-linear solver of the PETSc library [8, 9] has been applied to fulfill the bound of d.

3.2.6 HDF—Hybrid-Dimensional-Formulation

Hydro-mechanical modeling of fluid flow in deformable high aspect-ratio fractures (aperture $\ll$ fracture length) requires special numerical treatment of the governing equations. Discretization of high aspect-ratio fractures is challenging, and small absolute fracture deformations might lead to non-linear changes in the flow conditions within the fracture domain. Hybrid-dimensional elements were designed to overcome these difficulties and implicitly couple flow in deformable fractures with the deformation state of the surrounding matrix [24, 37, 38, 49, 50, 92–95, 97, 121–123].

Governing Equations of the Hybrid-Dimensional Formulation

Flow in hydraulic transmissive high aspect-ratio fractures is based on the physics of viscous fluids $Re \ll 1$ and creeping flow conditions resulting in a Poiseuille-type flow description [131]. The introduced assumptions simplify the balance of momentum to a pressure driven flow formulation where the relative fluid velocity

$$\mathbf{w}_\mathfrak{f} = -\frac{\delta(\mathbf{u})^2}{12\,\eta^{\mathfrak{f}R}} \operatorname{grad} p =: -\frac{k_{Fr}^{\mathfrak{s}}}{\eta^{\mathfrak{f}R}} \operatorname{grad} p, \tag{3.45}$$

is obtained from the parabolic velocity profile. In (3.45) δ denotes the fracture aperture, $\eta^{\mathfrak{f}R}$ the effective dynamic viscosity, $\mathbf{u}$ the fracture deformation, p the fluid pressure and $k_{Fr}^{\mathfrak{s}}$ the introduced local fracture permeability. To determine relations between injected fluid and fracture volume, fluid density changes and fluid velocity the balance of mass is evaluated for a compressible fluid in deformable fractures. Hence,

$$\dot{\overline{(\rho^{\mathfrak{f}R}\,\delta)}} + \operatorname{div}\left(\mathbf{w}_\mathfrak{f}\,\rho^{\mathfrak{f}R}\,\delta\right) = 0 \tag{3.46}$$

provides the condition to fulfill the conservation of mass in a deformable fracture setting, where $\rho^{\mathrm{f}R}$ is the fluid density. Once the fracture is surrounded by a porous medium leak-off can occur and is simply taken into account by an additional source term on the right hand side of (3.46). Evaluation of the balance of mass and momentum and assuming a linear constitutive relationship between fluid pressure and effective fluid density for barotropic fluids provides the scalar, lower-dimensional governing equation for fluid flow in deformable fractures

$$\underbrace{\dot{p}}_{(I)} \underbrace{- \frac{\delta^2}{12\,\eta^{\mathrm{f}R}} \operatorname{grad} p \cdot \operatorname{grad} p}_{(II)} \underbrace{- \frac{\delta}{12\,\eta^{\mathrm{f}R}\,\beta^{\mathrm{f}}} \operatorname{grad}\delta \cdot \operatorname{grad} p}_{(III)} \underbrace{- \frac{1}{12\;\eta^{\mathrm{f}R}\beta^{\mathrm{f}}} \operatorname{div}\left(\delta^2 \operatorname{grad} p\right)}_{(IV)} + \underbrace{\frac{1}{\delta\,\beta^{\mathrm{f}}} \frac{\partial \delta}{\partial t}}_{(V)} = \underbrace{q_{lk}}_{(VI)} \tag{3.47}$$

Equation (3.47) consists of a transient (*I*), a quadratic (*II*), a convection (*III*), a diffusion (*IV*), a coupling (*V*) and a leak-off (*VI*) term. Due to their minor contribution to the overall solution terms (*II*) and (*III*) will be neglected in the following.

Numerical Implementation

Different strategies to solve (3.47) have been proposed in the literature. Due to the stiff nature of the global system, implicit coupling of the rock matrix and fracture domain is mandatory. Solution strategies can be distinguished between staggered and monolithic approaches. Staggered algorithms allow calculations on independent domains and non-conformal meshing of fluid and solid domains [38], but require a higher number of iterations compared to the monolithic approaches [92]. Monolithic approaches such as zero-thickness interface elements are numerically stable and allow modeling of constitutive contact behavior of fracture surfaces since connectivity between both surfaces is guaranteed [95]. Here we focus on the element formulation of zero-thickness interface elements. The interested reader is referred to [37, 38, 92] for a detailed description of weak coupling schemes.

Interface elements allow longitudinal and transversal fracture flow as well as pressure jumps along both fracture surfaces. Numerically it is realized by auxiliary lower dimensional elements and averaging of the balance of mass and momentum. For the averaging process the already introduced balances of mass and momentum are extended to capture longitudinal and transversal fracture flow by decomposition of the seepage velocity

$$\mathbf{w}_{\mathrm{f}} = \mathbf{w}_{\mathrm{f}}^{l} + \mathbf{w}_{\mathrm{f}}^{t}. \tag{3.48}$$

In order to allow integration of aligning node values on auxiliary element level the balance of mass is averaged over the fracture height and reads

$$\frac{\delta}{K^{\mathfrak{f}}}\dot{P}_{\mathfrak{f}} + \dot{\delta} + \mathrm{div}_l\left(\mathbf{W}_{\mathfrak{f}}\delta\right) = \mathbf{w}_{\mathfrak{f}}^{+}\cdot\mathbf{n}^{+} + \mathbf{w}_{\mathfrak{f}}^{-}\cdot\mathbf{n}^{-} \tag{3.49}$$

where $P_{\mathfrak{f}} = \int_{-\delta/2}^{\delta/2}\hat{p}\,\mathrm{d}\mathbf{n}$ is the integral pressure, $\mathbf{W}_{\mathfrak{f}} = \int_{-\delta/2}^{\delta/2}\mathbf{w}_{\mathfrak{f}}^{t}\,\mathrm{d}\mathbf{n}$ the integral seepage velocity, $K^{\mathfrak{f}}$ the fluid's bulk modulus, div_l the divergence evaluated in longitudinal direction and the superscripts $^{+}$ and $^{-}$ denote the fracture surfaces. Averaging of the balance of momentum is conducted for the longitudinal and transversal fracture flow separately. In the longitudinal direction, the averaging process results in

$$\mathbf{W}_{\mathfrak{f}} = -\frac{k_{Fr,l}^{\mathfrak{s}}(\mathbf{x},t)}{\eta^{\mathfrak{f}R}}\,\mathrm{grad}_l\,P_{\mathfrak{f}}. \tag{3.50}$$

Description of the balance of momentum for transversal flow is realized by introducing and averaging a Darcy-like pressure-flow relationship which is approximated by the trapezoidal rule and finally given by

$$\frac{1}{2}\left(-\mathbf{w}_{\mathfrak{f}}^{+}\cdot\mathbf{n}^{+} + \mathbf{w}_{\mathfrak{f}}^{-}\cdot\mathbf{n}^{-}\right) = -\frac{k_{Fr,t}^{\mathfrak{s}}}{\eta^{\mathfrak{f}R}}\frac{-p^{+}+p^{-}}{\delta}. \tag{3.51}$$

A boundary condition for pressure $P_{\mathfrak{f}}$ closes the set of averaged balance equations. The formulation of the averaged quantity $P_{\mathfrak{f}}$ depends on the domain composition of the fracture height and reads

$$\begin{aligned} -\xi\,\mathbf{w}_{\mathfrak{f}}^{+}\cdot\mathbf{n}^{+} + \frac{2\,k_{Fr,t}^{\mathfrak{s}}}{\delta\,\eta^{\mathfrak{f}R}}p^{+} &= -(1-\xi)\,\mathbf{w}_{\mathfrak{f}}^{-}\cdot\mathbf{n}^{-} + \frac{2\,k_{Fr,t}^{\mathfrak{s}}}{\delta\,\eta^{\mathfrak{f}R}}P \\ -\xi\,\mathbf{w}_{\mathfrak{f}}^{-}\cdot\mathbf{n}^{-} + \frac{2\,k_{Fr,t}^{\mathfrak{s}}}{\delta\,\eta^{\mathfrak{f}R}}p^{-} &= -(1-\xi)\,\mathbf{w}_{\mathfrak{f}}^{+}\cdot\mathbf{n}^{+} + \frac{2\,k_{Fr,t}^{\mathfrak{s}}}{\delta\,\eta^{\mathfrak{f}R}}P \end{aligned} \tag{3.52}$$

in its general form. Here the stability limit $\xi = 1/2$ [93] is chosen [62] so that the pressure jump along the fracture height and averaged pressure P are given by

$$\begin{aligned} P_{\mathfrak{f}} &= \frac{p^{+}+p^{-}}{2} \\ \mathbf{w}_{\mathfrak{f}}^{-}\cdot\mathbf{n}^{-} - \mathbf{w}_{\mathfrak{f}}^{+}\cdot\mathbf{n}^{+} &= 2\,k_{Fr,t}^{\mathfrak{s}}\frac{p^{-}-p^{+}}{\delta}. \end{aligned} \tag{3.53}$$

The averaged governing equation for fluid flow in a deformable fracture at auxiliary element level is finally obtained by addition/subtraction of (3.49) and (3.53) and leads to

$$\begin{aligned}
&\frac{1}{2}\left[\frac{1}{K^{\mathfrak{f}}}\dot{P}_{\mathfrak{f}} + \dot{\delta} + \mathrm{div}_l\left(\mathbf{W}_{\mathfrak{f}}\delta\right)\right] - k^{\mathfrak{s}}_{Fr,t}\,P^t_{\mathfrak{f}} = \mathbf{w}^+_{\mathfrak{f}}\cdot\mathbf{n}^+ \quad \text{on } \Gamma^{Fr}_+,\\
&\frac{1}{2}\left[\frac{1}{K^{\mathfrak{f}}}\dot{P}_{\mathfrak{f}} + \dot{\delta} + \mathrm{div}_l\left(\mathbf{W}_{\mathfrak{f}}\delta\right)\right] + k^{\mathfrak{s}}_{Fr,t}\,P^t_{\mathfrak{f}} = \mathbf{w}^-_{\mathfrak{f}}\cdot\mathbf{n}^- \quad \text{on } \Gamma^{Fr}_-.
\end{aligned} \tag{3.54}$$

To solve the governing equation (3.54) in a finite element (FE) framework the weak form of the zero-thickness element formulation results in

$$\begin{aligned}
&\int_{\Gamma^{Fr}_+}\left[\frac{1}{2}\left(\dot{P}_{\mathfrak{f}}\,w_a + \frac{\delta^2}{12\,\eta^{\mathfrak{f}R}\beta^{\mathfrak{f}}}\mathrm{grad}_l\,P_{\mathfrak{f}}\cdot\mathrm{grad}_l\,w_a + \frac{1}{\delta\,\beta^{\mathfrak{f}}}\frac{\partial\delta}{\partial t}\,w_a\right) - \frac{1}{\delta\,\beta^{\mathfrak{f}}}\,k^{\mathfrak{s}}_{Fr,t}\,P^t_{\mathfrak{f}}\,w_a\right]\mathrm{d}v\\
&\quad = \frac{1}{\delta\,\beta^{\mathfrak{f}}}\,\mathbf{w}^+_{\mathfrak{f}}\cdot\mathbf{n}^+,\\
&\int_{\Gamma^{Fr}_-}\left[\frac{1}{2}\left(\dot{P}_{\mathfrak{f}}\,w_a + \frac{\delta^2}{12\,\eta^{\mathfrak{f}R}\beta^{\mathfrak{f}}}\mathrm{grad}_l\,P_{\mathfrak{f}}\cdot\mathrm{grad}_l\,w_a + \frac{1}{\delta\,\beta^{\mathfrak{f}}}\frac{\partial\delta}{\partial t}\,w_a\right) + \frac{1}{\delta\,\beta^{\mathfrak{f}}}\,k^{\mathfrak{s}}_{Fr,t}\,P^t_{\mathfrak{f}}\,w_a\right]\mathrm{d}v\\
&\quad = \frac{1}{\delta\,\beta^{\mathfrak{f}}}\,\mathbf{w}^-_{\mathfrak{f}}\cdot\mathbf{n}^-
\end{aligned} \tag{3.55}$$

where w_a is the lower dimensional test function used for the integration of the auxiliary elements. The form provided by Eq. (3.55) is implemented in a FE framework using a Newton-Raphson scheme to solve non-linear, transient pressure diffusion problems in deformable fractures surrounded by a porous matrix which is captured by Biot's theory.

References

1. S. Adami, X.Y. Hu, and Nikolaus A. Adams. A generalized wall boundary condition for smoothed particle hydrodynamics. *Journal of Computational Physics*, 231(21):7057–7075, 2012.
2. R. Alessi, M. Ambati, T. Gerasimov, S. Vidoli, and L. De Lorenzis. *Comparison of Phase-Field Models of Fracture Coupled with Plasticity*, pages 1–21. Springer International Publishing, Cham, 2018.
3. R. Alessi, J. J. Marigo, C. Maurini, and S. Vidoli. Coupling damage and plasticity for a phase-field regularisation of brittle, cohesive and ductile fracture: One-dimensional examples. *International Journal of Mechanical Sciences*, pages 1–18, 2017.
4. M. Ambati, T. Gerasimov, and L. De Lorenzis. Phase-field modeling of ductile fracture. *Computational Mechanics*, 55(5):1017–1040, 2015.
5. Hanen Amor, Jean-jacques Marigo, and Corrado Maurini. Regularized formulation of the variational brittle fracture with unilateral contact: numerical experiments. *Journal of Mechanics and Physics of Solids*, 57(8):1209–1229, 2009.
6. D. Asahina, J.E. Houseworth, J.T. Birkholzer, J. Rutqvist, and J.E. Bolander. Hydro-mechanical model for wetting/drying and fracture development in geomaterials. *Computers and Geosciences*, 65:13–23, 2014. cited By 30.
7. M. Bahrami, M.M. Yovanovich, and J.R. Culham. Effective thermal conductivity of rough spherical packed beds. *International Journal of Heat and Mass Transfer*, 49(19–20):3691–3701, 2006. cited By 110.

8. S. Balay, S. Abhyankar, M. F. Adams, J. Brown, P. Brune, K. Buschelman, L Dalcin, A. Dener, V. Eijkhout, W. D. Gropp, D. Karpeyev, D. Kaushik, M. G. Knepley, D. A. May, L. C. McInnes, R. T. Mills, T. Munson, K. Rupp, P. Sanan, B. F. Smith, S. Zampini, H. Zhang, and H. Zhang. PETSc Web page, 2019.
9. S. Balay, S. Abhyankar, M. F. Adams, J. Brown, P. Brune, K. Buschelman, L Dalcin, A. Dener, V. Eijkhout, W. D. Gropp, D. Karpeyev, D. Kaushik, M. G. Knepley, D. A. May, L. C. McInnes, R. T. Mills, T. Munson, K. Rupp, P. Sanan, B. F. Smith, S. Zampini, H. Zhang, and H. Zhang. PETSc users manual. Technical Report ANL-95/11—Revision 3.11, Argonne National Laboratory, 2019.
10. T. Belytschko and T. Black. Elastic crack growth in finite elements with minimal remeshing. *International Journal for Numerical Methods in Engineering*, 45(5):601–620, 1999. cited By 2659.
11. J.E. Bolander and S. Saito. Fracture analyses using spring networks with random geometry. *Engineering Fracture Mechanics*, 6:1569–1591, 1998.
12. J.E. Bolander Jr. and S. Saito. Fracture analyses using spring networks with random geometry. *Engineering Fracture Mechanics*, 61(5–6):569–591, 1998. cited By 322.
13. M.J. Borden, C.V. Verhoosel, M.A. Scott, T.J.R. Hughes, and C.M. Landis. A phase-field description of dynamic brittle fracture. *Computer Methods in Applied Mechanics and Engineering*, 217–220:77–95, 2012.
14. B. Bourdin, G.A. Francfort, and J.-J. Marigo. Numerical experiments in revisited brittle fracture. *Journal of the Mechanics and Physics of Solids*, 48(4):797–826, 2000. cited By 456.
15. B. Bourdin, G.A. Francfort, and J.-J. Marigo. Numerical experiments in revisited brittle fracture. *J. Mech. and Phys. of Solids*, 48(4):797–826, 2000.
16. B. Bourdin, G.A. Francfort, and J.-J. Marigo. The variational approach to fracture. *Journal of Elasticity*, 91(1-3):5–148, 2008.
17. B. Bourdin, C.J. Larsen, and C.L. Richardson. A time-discrete model for dynamic fracture based on crack regularization. *International Journal of Fracture*, 168(2):133–143, 2011.
18. Blaise Bourdin, Chukwudi P. Chukwudozie, and Keita Yoshioka. A Variational Approach to the Numerical Simulation of Hydraulic Fracturing. In *the 2012 SPE Annual Technical Conference and Exhibition*, 2012.
19. Blaise Bourdin, Jean Jacques Marigo, Corrado Maurini, and Paul Sicsic. Morphogenesis and propagation of complex cracks induced by thermal shocks. *Physical Review Letters*, 112(1):1–5, 2014.
20. H.H. Bui, J.K. Kodikara, A. Bouazza, A. Haque, and P.G. Ranjith. A novel computational approach for large deformation and post-failure analyses of segmental retaining wall systems. *International Journal for Numerical and Analytical Methods in Geomechanics*, 38(13):1321–1340, 2014. cited By 15.
21. H.H. Bui, K. Sako, and R. Fukagawa. Numerical simulation of soil-water interaction using smoothed particle hydrodynamics (sph) method. *Journal of Terramechanics*, 44(5):339–346, 2007. cited By 94.
22. T. Cajuhi, L. Sanavia, and Laura De Lorenzis. Phase-field modeling of fracture in variably saturated porous media. *Computational Mechanics*, pages 1–20, 2017.
23. Davide Casagrande, O Buzzi, Anna Giacomini, Cedric Lambert, and G Fenton. A new stochastic approach to predict peak and residual shear strength of natural rock discontinuities. *Rock Mechanics and Rock Engineering*, pages 69–99, 08 2017.
24. N. Castelletto, J. A. White, and H. A. Tchelepi. Accuracy and convergence properties of the fixed-stress iterative solution of two-way coupled poromechanics. *International Journal for Numerical and Analytical Methods in Geomechanics*, 39(14):1593–1618, 2015.
25. J. Chessa and T. Belytschko. An extended finite element method for two-phase fluids. *Journal of Applied Mechanics, Transactions ASME*, 70(1):10–17, 2003. cited By 195.
26. C. Chukwudozie, B. Bourdin, and K. Yoshioka. A variational phase-field model for hydraulic fracturing in porous media. *Computer Methods in Applied Mechanics and Engineering*, 347:957–982, 2019. cited By 6.

27. J. Chung, A. Roos, J.M. De Hosson, and E. van der Giessen. Fracture of disordered three-dimensional spring networks: A computer simulation methodology. *Physical Review B—Condensed Matter and Materials Physics*, 54(21):15094–15100, 1996. cited By 23.
28. P.A. Cundall and O.D.L. Strack. A discrete numerical model for granular assemblies. *Geotechnique*, 29(1):47–65, 1979. cited By 9142.
29. W.A. Curtin and H. Scher. Brittle fracture in disordered materials: A spring network model. *Journal of Materials Research*, 5(3):535–553, 1990. cited By 117.
30. P. Farrell and C. Maurini. Linear and nonlinear solvers for variational phase-field models of brittle fracture. *International Journal for Numerical Methods in Engineering*, 109(5):648–667, 2017.
31. Ali Fathi, Zabihallah Moradian, Patrice Rivard, Gérard Ballivy, and Andrew J. Boyd. Geometric effect of asperities on shear mechanism of rock joints. *Rock Mechanics and Rock Engineering*, 49(3):801–820, Mar 2016.
32. Y.T. Feng, K. Han, C.F. Li, and D.R.J. Owen. Discrete thermal element modeling of heat conduction in particle systems: Basic formulations. *Journal of Computational Physics*, 227:5072–5089, 2008.
33. B. Flemisch, M. Darcis, K. Erbertseder, B. Faigle, A. Lauser, K. Mosthaf, S. Müthing, P. Nuske, A. Tatomir, M. Wolff, and R. Helmig. Dumux: Dune for multi-phase,component,scale,physics,... flow and transport in porous media. *Advances in Water Resources*, 34(9):1102–1112, 2011. cited By 138.
34. G.A. Francfort and J.-J Marigo. Revisiting brittle fracture as an energy minimization problem. *J. Mech. and Phys. of Solids*, 46(8):1319–1342, 1998.
35. T. Gerasimov and L. De Lorenzis. A line search assisted monolithic approach for phase-field computing of brittle fracture. *Computer Methods in Applied Mechanics and Engineering*, 312:276 – 303, 2016. Phase Field Approaches to Fracture.
36. Robert A Gingold and Joseph J Monaghan. Smoothed particle hydrodynamics: theory and application to non-spherical stars. *Monthly notices of the royal astronomical society*, 181(3):375–389, 1977.
37. V. Girault, M. F. Wheeler, B. Ganis, and M. E. Mear. A lubrication fracture model in a poroelastic medium. *Mathematical Models and Methods in Applied Sciences*, 25(4):587–645, 2015.
38. Vivette Girault, Kundan Kumar, and Mary F. Wheeler. Convergence of iterative coupling of geomechanics with flow in a fractured poroelastic medium. *Computational Geosciences*, 20(5):997–1011, Oct 2016.
39. P. Grassl. A lattice approach to model flow in cracked concrete. *Cement & Concrete Composites*, 31:454–460, 2009.
40. P. Grassl, C. Fahy, D. Gallipoli, and J. Bolander. A lattice model for liquid transport in cracked unsaturated heterogeneous porous materials. *VIII International Conference on Fracture Mechanics of Concrete and Concrete Structures*, 2013.
41. V. Hakim and A. Karma. Laws of crack motion and phase-field models of fracture. *Journal of the Mechanics and Physics of Solids*, 57(2):342–368, 2009.
42. Alan Thomas Joseph Hayward. Compressibility equations for liquids: a comparative study. *British Journal of Applied Physics*, 18(7):965, 1967.
43. Y. Heider and B. Markert. A phase-field modeling approach of hydraulic fracture in saturated porous media. *Mechanics Research Communications*, 80:38–46, 2017. cited By 34.
44. M. Hofacker and C. Miehe. Continuum phase field modeling of dynamic fracture: Variational principles and staggered FE implementation. *International Journal of Fracture*, 178(1–2):113–129, 2012.
45. R. Ince, A. Arslan, and B.L. Karihaloo. Lattice modelling of size effect in concrete strength. *Engineering Fracture Mechanics*, 70:2307–2320, 2003.
46. A. Jagota and G.W. Scherer. Viscosities and sintering rates of a two-dimensional granular composite. *Journal of the American Ceramic Society*, 76(12):3123–3135, 1993. cited By 40.
47. B.L. Karihaloo, P.F. Shao, and Q.Z. Xiao. Lattice modelling of the failure of particle composites. *Engineering Fracture Mechanics*, 70:2385–2406, 2003.

48. A.R. Khoei, S. Moallemi, and E. Haghighat. Thermo-hydro-mechanical modeling of impermeable discontinuity in saturated porous media with x-fem technique. *Engineering Fracture Mechanics*, 96:701–723, 2012. cited By 28.
49. J. Kim, H.A. Tchelepi, and R. Juanes. Stability and convergence of sequential methods for coupled flow and geomechanics: Drained and undrained splits. *Computer Methods in Applied Mechanics and Engineering*, 200(23):2094 – 2116, 2011.
50. J. Kim, H.A. Tchelepi, and R. Juanes. Stability and convergence of sequential methods for coupled flow and geomechanics: Fixed-stress and fixed-strain splits. *Computer Methods in Applied Mechanics and Engineering*, 200(13):1591 – 1606, 2011.
51. Markus Klinsmann, Daniele Rosato, Marc Kamlah, and Robert M. McMeeking. An assessment of the phase field formulation for crack growth. *Computer Methods in Applied Mechanics and Engineering*, 294(Supplement C):313 – 330, 2015.
52. O. Kolditz, S. Bauer, C. Beyer, N. Böttcher, P. Dietrich, U.-J. Görke, T. Kalbacher, C.-H. Park, U. Sauer, C. Schütze, H. Shao, A. Singh, J. Taron, W. Wang, and N. Watanabe. A systematic benchmarking approach for geologic CO2 injection and storage. *Environmental Earth Sciences*, 67(2):613–632, 2012.
53. C. Kuhn and R. Müller. A continuum phase field model for fracture. *Engineering Fracture Mechanics*, 77(18):3625–3634, 2010.
54. C. Kuhn, T. Noll, and R. Müller. On phase field modeling of ductile fracture. *GAMM Mitteilungen*, 39(1):35–54, 2016.
55. K. Li and S. Zhou. Numerical investigation of multizone hydraulic fracture propagation in porous media: New insights from a phase field method. *Journal of Natural Gas Science and Engineering*, 66:42–59, 2019. cited By 2.
56. T. Li, J.-J. Marigo, D. Guilbaud, and S. Potapov. Gradient damage modeling of brittle fracture in an explicit dynamic context. *International Journal for Numerical Methods in Engineering*, 00(March):1–25, 2016.
57. A. Lisjak, P. Kaifosh, L. Hea, B.S.A. Tatone, O.K. Mahabadi, and G. Grasselli. A 2d, fully-coupled, hydro-mechanical, fdem formulation for modelling fracturing processes in discontinuous, porous rock masses. *Computers and Geotechnics*, 81:1–18, 2017.
58. J.X. Liu, S.C. Deng, J. Zhang, and N.G Liang. Lattice type of fracture model for concrete. *Theoretical and Applied Fracture Mechanics*, 48:269–284, 2007.
59. Leon B Lucy. A numerical approach to the testing of the fission hypothesis. *The astronomical journal*, 82:1013–1024, 1977.
60. J.-J. Marigo, C. Maurini, and K. Pham. An overview of the modelling of fracture by gradient damage models. *Meccanica*, 51(12):3107–3128, 2016.
61. D Markauskas, H Kruggel-Emden, R Sivanesapillai, and H Steeb. Comparative study on mesh-based and mesh-less coupled cfd-dem methods to model particle-laden flow. *Powder Technology*, 305:78–88, 2017.
62. V. Martin, J. Jaffré, and J. Roberts. Modeling fractures and barriers as interfaces for flow in porous media. *SIAM Journal on Scientific Computing*, 26(5):1667–1691, 2005.
63. C. Maurini, B. Bourdin, G. Gauthier, and V. Lazarus. Crack patterns obtained by unidirectional drying of a colloidal suspension in a capillary tube: Experiments and numerical simulations using a two-dimensional variational approach. *International Journal of Fracture*, 184(1–2):75–91, 2013.
64. P. Meakin. Models for material failure and deformation. *Science*, 252(5003):226–234, 1991. cited By 104.
65. G. Meschke and D. Leonhart. A generalized finite element method for hydro-mechanically coupled analysis of hydraulic fracturing problems using space-time variant enrichment functions. *Computer Methods in Applied Mechanics and Engineering*, 290:438–465, 2015. cited By 19.
66. C. Miehe, M. Hofacker, L. M. Schänzel, and F. Aldakheel. Phase field modeling of fracture in multi-physics problems. Part II. Coupled brittle-to-ductile failure criteria and crack propagation in thermo-elastic-plastic solids. *Computer Methods in Applied Mechanics and Engineering*, 294:486–522, 2015.

67. C. Miehe, M. Hofacker, L.-M. Schänzel, and F. Aldakheel. Phase field modeling of fracture in multi-physics problems. part ii. coupled brittle-to-ductile failure criteria and crack propagation in thermo-elastic-plastic solids. *Computer Methods in Applied Mechanics and Engineering*, 294:486–522, 2015. cited By 103.
68. C. Miehe, F. Welschinger, and M. Hofacker. Thermodynamically consistent phase-field models of fracture: Variational principles and multi-field fe implementations. *International Journal for Numerical Methods in Engineering*, 83(10):1273–1311, 2010.
69. T. Mohammadnejad and A.R. Khoei. An extended finite element method for fluid flow in partially saturated porous media with weak discontinuities; the convergence analysis of local enrichment strategies. *Computational Mechanics*, 51(3):327–345, 2013. cited By 26.
70. J.J. Monaghan. Smoothed particle hydrodynamics and its diverse applications. *Annual Review of Fluid Mechanics*, 44:323–346, 2011. cited By 306.
71. Joe J Monaghan. Smoothed particle hydrodynamics. *Annual review of astronomy and astrophysics*, 30(1):543–574, 1992.
72. Joseph J Monaghan. Smoothed particle hydrodynamics and its diverse applications. *Annual Review of Fluid Mechanics*, 44:323–346, 2012.
73. J.P. Morris. Simulating surface tension with smoothed particle hydrodynamics. *International Journal for Numerical Methods in Fluids*, 33(3):333–353, 2000. cited By 272.
74. C. Moukarzel and H. J. Herrmann. A vectorizable random lattice. *J. Stat. Phys.*, 68:911–923, 1992.
75. M. Ostoja-Starzewski. Lattice models in micromechanics. *Applied mechanics*, 55(1):35–60, 2002.
76. K. Pham, H. Amor, J.-J. Marigo, and C. Maurini. Gradient damage models and their use to approximate brittle fracture. *Int. J. Damage Mech.*, 20(4, SI):618–652, 2011.
77. E.P. Prado and J.G.M. van Mier. Effect of particle structure on mode i fracture process in concrete. *Engineering Fracture Mechanics*, 70:1793–1807, 2003.
78. K. Pruess. The tough codes-a family of simulation tools for multiphase flow and transport processes in permeable media. *Vadose Zone Journal*, 3(3):738–746, 2004. cited By 201.
79. Z. H. Rizvi, M. Nikolic, and F. Wuttke. Lattice element method for simulations of failure in bio-cemented sands. *Granular Matter*, 21(18), 2019.
80. Z.H. Rizvi, A.S. Sattari, and F. Wuttke. Numerical analysis of heat conduction in granular geo-material using lattice element method. *Energy Geotechnics—Proceedings of the 1st International Conference on Energy Geotechnics, ICEGT*, pages 367–372, 2016.
81. Z.H. Rizvi, A.S. Sattari, and F. Wuttke. Meso scale modelling of infill foam concrete wall for earthquake loads. *16th European Conference on Earthquake Engineering (16ECEE), Thessaloniki, Greece*, 2018.
82. Z.H. Rizvi, K. Sembdner, A. Suman, M.J. Giri Prasad, and F. Wuttke. Experimental and numerical investigation of thermo-mechanical properties for nano-geocomposite. *International Journal of Thermophysics*, 40(5), 2019. cited By 1.
83. Z.H. Rizvi, D. Shrestha, A.S. Sattari, and F. Wuttke. Numerical modelling of effective thermal conductivity for modified geomaterial using lattice element method. *Heat Mass Transf*, 54(2):483–499, 2018.
84. Z.H. Rizvi, F. Wuttke, and A.S. Sattari. Dynamic analysis by lattice element method simulation. *Springer Series in Geomechanics and Geoengineering*, (216849):405–409, 2018. cited By 2.
85. M. Sahimi and S. Arbabi. Mechanics of disordered solids. iii. fracture properties. *Physical Review B*, 47(2):713–722, 1993. cited By 80.
86. D. Santillán, R. Juanes, and L. Cueto-Felgueroso. Phase field model of fluid-driven fracture in elastic media: Immersed-fracture formulation and validation with analytical solutions. *Journal of Geophysical Research: Solid Earth*, 2017.
87. J.M. Sargado, E. Keilegavlen, I. Berre, and J.M. Nordbotten. High-accuracy phase-field models for brittle fracture based on a new family of degradation functions. *Journal of the Mechanics and Physics of Solids*, 111:458–489, 2018.

88. A. S. Sattari, H. B. Motra, Z. H. Rizvi, and F. Wuttke. A new lattice element method (lem) with integrated interface elements for determining the effective thermal conductivity of rock solids under thermo-mechanical processes. *International Symposium on Energy Geotechnics (SEG), Energy Geotechnics*, pages 266–275, 2019.
89. A.S. Sattari, Z.H. Rizvi, H.B. Motra, and F. Wuttke. Meso-scale modeling of heat transport in a heterogeneous cemented geomaterial by lattice element method. *Granular Matter*, 19(66), 2017.
90. E. Schlangen and J.G.M. Van Mier. Micromechanical analysis of fracture of concrete. *International Journal of Damage Mechanics*, 1(4):435–454, 1992. cited By 33.
91. A. Schlüter, A. Willenbücher, C. Kuhn, and R. Müller. Phase field approximation of dynamic brittle fracture. *Computational Mechanics*, 54(5):1141–1161, 2014.
92. P. Schmidt and H. Steeb. Numerical aspects of hydro-mechanical coupling of fluid-filled fractures using hybrid-dimensional element formulations and non-conformal meshes. *Int J Geomath*, 10(14), 2019.
93. J. M. Segura and I. Carol. On zero-thickness interface elements for diffusion problems. *International Journal for Numerical and Analytical Methods in Geomechanics*, 28(9):947–962, 2004.
94. J Ma Segura and I Carol. Coupled hm analysis using zero-thickness interface elements with double nodes. Part I: Theoretical model. *International journal for numerical and analytical methods in geomechanics*, 32(18):2083–2101, 2008.
95. JM Segura and I Carol. Coupled hm analysis using zero-thickness interface elements with double nodes. Part II: Verification and application. *International Journal for Numerical and Analytical Methods in Geomechanics*, 32(18):2103–2123, 2008.
96. M. Seiler, P. Hantschke, A. Brosius, and M. Kästner. A numerically efficient phase-field model for fatigue fracture - 1D analysis. *Pamm*, 18(1):e201800207, 2018.
97. Randolph R Settgast, Pengcheng Fu, Stuart DC Walsh, Joshua A White, Chandrasekhar Annavarapu, and Frederick J Ryerson. A fully coupled method for massively parallel simulation of hydraulically driven fractures in 3-dimensions. *International Journal for Numerical and Analytical Methods in Geomechanics*, 41(5):627–653, 2017.
98. Q. Shao, L. Bouhala, A. Younes, P. Núñez, A. Makradi, and S. Belouettar. An xfem model for cracked porous media: Effects of fluid flow and heat transfer. *International Journal of Fracture*, 185(1–2):155–169, 2014. cited By 9.
99. D. Shrestha, Z.H. Rizvi, and F. Wuttke. Effective thermal conductivity of unsaturated granular geocomposite using lattice element method. *Heat and Mass Transfer*, 55(6):1671–1683, 2019.
100. J. Sima, M. Jiang, and C. Zhou. Modelling desiccation cracking in thin clay layer using three-dimensional discrete element method. *AIP Conference Proceedings*, 1542(1), 2013.
101. R. Sivanesapillai, N. Falkner, A. Hartmaier, and H. Steeb. A csf-sph method for simulating drainage and imbibition at pore-scale resolution while tracking interfacial areas. *Advances in Water Resources*, 95:212–234, 2016. cited By 16.
102. R Sivanesapillai, H Steeb, and A Hartmaier. Transition of effective hydraulic properties from low to high reynolds number flow in porous media. *Geophysical Research Letters*, 41(14):4920–4928, 2014.
103. Rakulan Sivanesapillai. Pore-scale study of non-darcian fluid flow in porous media using smoothed-particle hydrodynamics. 2016.
104. Rakulan Sivanesapillai, Nadine Falkner, Alexander Hartmaier, and Holger Steeb. A csf-sph method for simulating drainage and imbibition at pore-scale resolution while tracking interfacial areas. *Advances in water resources*, 95:212–234, 2016.
105. Rakulan Sivanesapillai and Holger Steeb. Fluid interfaces during viscous-dominated primary drainage in 2d micromodels using pore-scale sph simulations. *Geofluids*, 2018, 2018.
106. H Steeb. Hydro-mechanics of porous and granular material—Poro-elasticity and beyond. In *Proceedings of Alert Workshop and School*. 2019.
107. H Steeb and J Renner. Mechanics of poro-elastic media: A review with emphasis on foundational state variables. *Transport in Porous Media*, 130:437–461, 2019.

108. T. Strouboulis, I. Babuška, and K. Copps. The design and analysis of the generalized finite element method. *Computer Methods in Applied Mechanics and Engineering*, 181(1–3):43–69, 2000. cited By 543.
109. William C Swope, Hans C Andersen, Peter H Berens, and Kent R Wilson. A computer simulation method for the calculation of equilibrium constants for the formation of physical clusters of molecules: Application to small water clusters. *The Journal of Chemical Physics*, 76(1):637–649, 1982.
110. R. Talreja. Continuum modelling of damage in ceramic matrix composites. *Mechanics of Materials*, 12(2):165–180, 1991. cited By 84.
111. E. Tanné, T. Li, B. Bourdin, J-J. Marigo, and C. Maurini. Crack nucleation in variational phase-field models of brittle fracture. *J. Mech. Phys. Solids*, 110:80–99, 2018.
112. A.M. Tartakovsky and P. Meakin. A smoothed particle hydrodynamics model for miscible flow in three-dimensional fractures and the two-dimensional rayleigh-taylor instability. *Journal of Computational Physics*, 207(2):610–624, 2005. cited By 127.
113. J. van der Lee, L. De Windt, V. Lagneau, and P. Goblet. Presentation and application of the reactive transport code hytec. *Developments in Water Science*, 47(C):599–606, 2002. cited By 17.
114. J.G.M. van Mier, M.R.A. van Vliet, and K. Wang Tai. Fracture mechanisms in particle composites: statistical aspects in lattice type analysis. *Mechanics of Materials*, 34, 2002.
115. W.L. Vargas and J.J. McCarthy. Heat conduction in granular materials. *AIChE Journal*, 47(5):1052–1059, 2001. cited By 154.
116. W.L. Vargas and J.J. McCarthy. Stress effects on the conductivity of particulate beds. *Chemical Engineering Science*, 57(15):3119–3131, 2002. cited By 61.
117. W.L. Vargas and J.J. McCarthy. Thermal expansion effects and heat conduction in granular materials. *Physical Review E—Statistical, Nonlinear, and Soft Matter Physics*, 76(4), 2007. cited By 43.
118. C.V. Verhoosel and R. de Borst. A phase-field model for cohesive fracture. *International Journal for Numerical Methods in Engineering*, 00:1–20, 2010.
119. Loup Verlet. Computer "experiments" on classical fluids. i. thermodynamical properties of lennard-jones molecules. *Physical review*, 159(1):98, 1967.
120. Julien Vignollet, Stefan May, René de Borst, and Clemens V. Verhoosel. Phase-field models for brittle and cohesive fracture. *Meccanica*, 49(11):2587–2601, 2014.
121. C Vinci, J Renner, and H Steeb. A hybrid-dimensional approach for an efficient numerical modeling of the hydro-mechanics of fractures. *Water Resources Research*, 50(2):1616–1635, 2014.
122. C. Vinci, H. Steeb, and J. Renner. The imprint of hydro-mechanics of fractures in periodic pumping tests. *Geophysical Journal International*, 202(3):1613–1626, 2015.
123. Carlo Vinci. *Hydro-mechanical coupling in fractured rocks: modeling and numerical simulations*. PhD thesis, Ruhr-University Bochum, 2014.
124. T.D. Vo, A. Pouya, S. Hemmati, and A.M. Tang. Numerical modelling of desiccation cracking of clayey soil using a cohesive fracture method. *Computers and Geotechnics*, 85:15–27, 2017.
125. W. Wang, T. Fischer, B. Zehner, N. Böttcher, U.-J. Görke, and O. Kolditz. A parallel finite element method for two-phase flow processes in porous media: Opengeosys with petsc. *Environmental Earth Sciences*, 73(5):2269–2285, 2015. cited By 12.
126. N. Watanabe, W. Wang, J. Taron, U.J. Görke, and O. Kolditz. Lower-dimensional interface elements with local enrichment: Application to coupled hydro-mechanical problems in discretely fractured porous media. *International Journal for Numerical Methods in Engineering*, 90(8):1010–1034, 2012. cited By 52.
127. H. Wei, J.-S. Chen, F. Beckwith, and J. Baek. A naturally stabilized semi-lagrangian meshfree formulation for multiphase porous media with application to landslide modeling. *Journal of Engineering Mechanics*, 146(4), 2020. cited By 1.
128. M.F. Wheeler, T. Wick, and W Wollner. An augmented-Lagrangian method for the phase-field approach for pressurized fractures. *Computer Methods in Applied Mechanics and Engineering*, 271:69–85, 2014.

129. G. Widenfeld, Y. Weiss, and H. Kalman. The effect of compression and preconsolidation on the effective thermal conductivity of particulate beds. *Powder Technology*, 133(1–3):15–22, 2003. cited By 19.
130. Z.A. Wilson and C.M. Landis. Phase-field modeling of hydraulic fracture. *Journal of the Mechanics and Physics of Solids*, 96:264–290, 2016.
131. P. A. Witherspoon, C. H. Amick, J. E. Gale, and K. Iwai. Observations of a potential size effect in experimental determination of the hydraulic properties of fractures. *Water Resources Research*, 15(5):1142–1146, 1979.
132. J.K.-W. Wong, K. Soga, X. Xu, and J.-Y. Delenne. Modelling fracturing process of geomaterial using lattice element method. *Geomechanics from Micro to Macro—Proceedings of the TC105 ISSMGE International Symposium on Geomechanics from Micro to Macro, IS-Cambridge 2014*, 1:417–422, 2015. cited By 2.
133. W. Woodside and J.H. Messmer. Thermal conductivity of porous media. i. unconsolidated sands. *Journal of Applied Physics*, 32(9):1688–1699, 1961. cited By 543.
134. J.-Y. Wu. A unified phase-field theory for the mechanics of damage and quasi-brittle failure. *Journal of the Mechanics and Physics of Solids*, 103:72–99, 2017.
135. Y.-S. Wu, K. Zhang, C. Ding, K. Pruess, E. Elmroth, and G.S. Bodvarsson. An efficient parallel-computing method for modeling nonisothermal multiphase flow and multicomponent transport in porous and fractured media. *Advances in Water Resources*, 25(3):243–261, 2002. cited By 51.
136. F. Wuttke, A.S. Sattari, Z.H. Rizvi, and H.B. Motra. Advanced meso-scale modelling to study the effective thermo-mechanical parameter in solid geomaterial. *Springer Series in Geomechanics and Geoengineering*, pages 85–95, 2017. cited By 10.
137. A. Yazid, N. Abdelkader, and H. Abdelmadjid. A state-of-the-art review of the x-fem for computational fracture mechanics. *Applied Mathematical Modelling*, 33(12):4269–4282, 2009. cited By 83.
138. T. Ye, D. Pan, C. Huang, and M. Liu. Smoothed particle hydrodynamics (SPH) for complex fluid flows: Recent developments in methodology and applications. *Physics of Fluids*, 31(011301), 2019.
139. K. Yoshioka, F. Parisio, D. Naumov, R. Lu, O. Kolditz, and T. Nagel. Comparative verification of discrete and smeared numerical approaches for the simulation of hydraulic fracturing. *GEM - International Journal on Geomathematics*, 10(1), 2019.
140. C. Zeeb and H. Konietzky. Simulating the hydraulic stimulation of multiple fractures in an anisotropic stress field applying the discrete element method. *Energy Procedia*, 76:264–272, 2015. cited By 10.
141. H.W. Zhang, Q. Zhou, H.L. Xing, and H. Muhlhaus. A dem study on the effective thermal conductivity of granular assemblies. *Powder Technology*, 205(1–3):172–183, 2011. cited By 55.
142. H.W. Zhang, Q. Zhou, H.L. Xing, and H. Muhlhaus. A dem study on the effective thermal conductivity of granular assemblies. *Powder Technology*, 205:172–183, 2011.
143. Minkley, W., Knauth, M., Wüste, U. (2012): Integrity of salinar barriers under consideration of discontinuum-mechanical aspects. Mechanical Behavior of Salt VII, Paris, France, 16–19 April 2012, 469–478. Taylor & Francis Group, London, ISBN 978-0-415-62122-9
144. Knauth,M. and Minkley,W. (2014): Modeling of themechanical and hydraulic behavior of salt rocks on discontinuum mechanical basis. Copyright 2014 ARMA, American Rock Mechanics Association. This paper was prepared for presentation at the 48thUS Rock Mechanics / Geomechanics Symposium held in Minneapolis, MN, USA, 1–4 June 2014, ARMA 14-7036
145. Minkley, W., Knauth, M., Brückner, D. (2013): Discontinuum-mechanical behaviour of salt rocks and the practical relevance for the integrity of salinar barriers. ARMA, 47th US Rock Mechanics Symposium, San Francisco, CA, USA, 23–26 June 2013. Paper ARMA 13-388
146. Minkley, W. and Mühlbauer, J. (2007): Constitutive models to describe themechanical behavior of salt rocks and the imbedded weakness planes. In: M. Wallner, K.H. Lux, W. Minkley & H. R. Hardy. The Mechanical Behavior of Salt - Understanding of THMC Processes in Salt: 6th Conference (SaltMech6), Hannover, Germany, 22–25 May 2007. Publ.: Taylor and Francis, ISBN: 9780415443982, 119–127.

147. Knauth, M. (2018): Diskontinuumsmechanische Modellierung von Salzgesteinen. Dissertation TU Bergakademie Freiberg